

# Titanium alkoxide induced BiOBr–Bi<sub>2</sub>WO<sub>6</sub> mesoporous nanosheet composites with much enhanced photocatalytic activity†

Cite this: *J. Mater. Chem. A*, 2013, **1**, 7949

Yongli Li,<sup>ab</sup> Yuanming Liu,<sup>c</sup> Jinshu Wang,<sup>\*a</sup> Evan Uchaker,<sup>b</sup> Qifeng Zhang,<sup>b</sup> Shibing Sun,<sup>a</sup> Yunxia Huang,<sup>b</sup> Jianguyu Li<sup>c</sup> and Guozhong Cao<sup>\*b</sup>

Here we report a facile hydrothermal route for the preparation of BiOBr–Bi<sub>2</sub>WO<sub>6</sub> mesoporous nanosheet composites (MNCs) in the presence of titanium isopropoxide, Ti(O<sup>i</sup>Pr)<sub>4</sub>. High resolution transmission electron microscopy, X-ray diffraction, nitrogen adsorption/desorption analysis and X-ray photoelectron spectroscopy were employed for structural and composition analyses of the MNCs. The photogenerated charge transfer and photocatalytic activity of BiOBr–Bi<sub>2</sub>WO<sub>6</sub> MNCs were investigated by Kelvin probe force microscopy and UV-vis spectroscopy. We propose mechanisms to illustrate how titanium alkoxide induces the formation of mesoporous nanosheet heterostructures and the enhanced photodecomposition efficiency of the dye under low light intensity illumination. Overall, our results suggest that titanium alkoxide is not only strongly involved in the growth of BiOBr (001) facets, but also plays a critical role in the pore evolution of the product. Kelvin probe force microscopy analysis allows us to conclude that the resulting nanocomposites demonstrate high photogenerated charge mobility and a long lifetime. Dye molecules can be rapidly and thoroughly decomposed with the photocatalyst under very low light intensity illumination. The enhanced photocatalytic activity is attributed to well matched band edge positions of BiOBr and Bi<sub>2</sub>WO<sub>6</sub> and the large specific surface area of the MNCs in view of the incorporation of mesopores and the highly exposed BiOBr (001) facet due to the use of Ti(O<sup>i</sup>Pr)<sub>4</sub> during the synthesis. The results presented here are expected to make a contribution toward the development of delicate nanocomposites for photocatalytic water purification and solar energy utilization.

Received 5th March 2013

Accepted 28th April 2013

DOI: 10.1039/c3ta10940b

[www.rsc.org/MaterialsA](http://www.rsc.org/MaterialsA)

## 1 Introduction

Semiconductor photocatalysts are desirable in many applications that cope with environmental and energy problems, which include removal of pollutants, antibiosis, water splitting, dye-sensitized solar cells, carbon dioxide reduction and artificial photosynthesis.<sup>1–6</sup> When a semiconductor photocatalyst

captures incident photons, electron–hole pairs (excitons) are produced when the energy of photons exceeds the band gap of the semiconductor. However, only a certain fraction of the electron–hole pairs can spatially separate to generate radical species on the semiconductor surface, where a redox reaction takes place. Therefore, the photocatalytic activity of a semiconductor is strongly dependent on the charge separation efficiency and the number of reactive sites on the semiconductor surface.<sup>7–10</sup> One of the most notable photocatalysts is TiO<sub>2</sub>, which however has limitations in visible light absorption.<sup>11,12</sup> BiOBr (bismuth oxybromide) as a relatively new member of the family of photocatalysts has been demonstrated to be a promising photocatalyst that has suitable band gap, can degrade a wide range of toxic organic pollutants and metal ions in water under visible light illumination, and shows good chemical stability and is eco-friendly.<sup>13–17</sup> Previous studies have revealed that the photocatalytic activity of BiOBr is determined by not only the surface atomic structure, but also the grain size, morphology and structure, and dominantly exposed facets.<sup>18–23</sup> It was suggested that if the charge recombination could be significantly reduced and meanwhile a high specific surface area could be maintained for the adsorption of reagents, good

<sup>a</sup>School of Materials Science and Engineering, Beijing University of Technology, Beijing 100124, China. E-mail: [lylbjut@gmail.com](mailto:lylbjut@gmail.com); [wangjsh@bjut.edu.cn](mailto:wangjsh@bjut.edu.cn); Fax: +86-67391101; Tel: +86-67391101

<sup>b</sup>Department of Materials Science and Engineering, University of Washington, Seattle, Washington 98195-2120, USA. E-mail: [gzaoc@u.washington.edu](mailto:gzaoc@u.washington.edu); Fax: +1-206-543-3100; Tel: +1-206-616-9084

<sup>c</sup>Department of Mechanical Engineering, University of Washington, Seattle, Washington 98195-2600, USA

† Electronic supplementary information (ESI) available: XPS and EDS analysis of BiOBr–Bi<sub>2</sub>WO<sub>6</sub> MNCs, XRD patterns of the MNCs with different fractions of Ti(O<sup>i</sup>Pr)<sub>4</sub>, XRD pattern of the MNCs with TBT as the Ti source, SEM images of the MNCs with different fractions of Ti(O<sup>i</sup>Pr)<sub>4</sub>, schematics of the KPFM measurement for photoinduced surface charge, UV-vis spectra of the materials, UV-vis spectral profile variation of RhB aqueous solution after degradation under visible light irradiation and photodegradation of MO in the presence of MNCs as referenced in the text. See DOI: 10.1039/c3ta10940b

photocatalytic activity should be obtained.<sup>21,22</sup> Recently, coupling BiOBr with other semiconductors, such as TiO<sub>2</sub>,<sup>24</sup> C<sub>3</sub>N<sub>4</sub>,<sup>25</sup> BiOI,<sup>26</sup> AgBr,<sup>27</sup> and CdS,<sup>28</sup> with matched energetic levels of valence band (VB) and conduction band (CB) has proved to be effective in facilitating charge separation, and consequently improving the photocatalytic performance. Morphology-controlled synthesis of BiOBr such as assembled nanosheet 3-dimensional structure has been studied for the quadratic growth of specific area and high-density reactive sites.<sup>19,21,29–31</sup> However, most work in the literature is based on high light intensity illumination of 50–100 mL aqueous solution with power supply from, for example, a 300–500 W Xe lamp,<sup>17,19,20,24,32,33</sup> which is much higher than the indoor light intensity and also higher than the outdoor sunlight intensity in most cases, limiting the practical application of these photocatalysts. Mesoporous structured nanocomposites of BiOBr coupled with Bi<sub>2</sub>WO<sub>6</sub> with high surface areas are promising materials that can increase light harvesting, enhance electron-hole separation, and thus achieve high photocatalytic efficiency.

This work introduces a direct hydrothermal synthesis of BiOBr–Bi<sub>2</sub>WO<sub>6</sub> mesoporous nanosheet composites (MNCs) with high surface areas and highly exposed BiOBr (001) facets by using Ti(O<sup>i</sup>Pr)<sub>4</sub> as a catalytic additive and cetyltrimethylammonium bromide (CTAB) as both Br precursor and surfactant. Bismuth tungstate, Bi<sub>2</sub>WO<sub>6</sub>, was chosen to couple with the BiOBr based on the following considerations: (1) Bi<sub>2</sub>WO<sub>6</sub> possesses a layered structure consisting of an alternating arrangement of [Bi<sub>2</sub>O<sub>2</sub>] sheets and WO<sub>6</sub> octahedra, which is similar to that of tetragonal BiOBr crystals.<sup>15–18,34–36</sup> As a result, it is possible for these two semiconductors to form an intimate contact through sharing the [Bi<sub>2</sub>O<sub>2</sub>] unit, (2) both BiOBr and Bi<sub>2</sub>WO<sub>6</sub> have been proven to perform excellently in the photocatalytic degradation of pollutants,<sup>20,37</sup> (3) they have similar band gaps,<sup>13,38</sup> and (4) both BiOBr and Bi<sub>2</sub>WO<sub>6</sub> can form hierarchical microspheres several tens of micrometers in size through a hydrothermal method,<sup>18–21,36–39</sup> which enables the materials to be separated and recycled for water treatment *via* filtration or sedimentation. The method that we developed is simple and mild, and can control the composition of nanostructures and the exposed facets. The nanostructure consists of a stack of nanosheets with a large number of mesopores. In view of their superior properties, the BiOBr–Bi<sub>2</sub>WO<sub>6</sub> MNCs developed in this study hold great promise for water treatment and photocatalysis.

## 2 Experimental section

### 2.1 Materials

Sodium tungstate dihydrate, Na<sub>2</sub>WO<sub>4</sub>·2H<sub>2</sub>O (99.5%), bismuth nitrate pentahydrate, Bi(NO<sub>3</sub>)<sub>3</sub>·5H<sub>2</sub>O (98%), (1-hexadecyl)trimethylammonium bromide (CTAB), C<sub>16</sub>H<sub>33</sub>(CH<sub>3</sub>)<sub>3</sub>NBr (98%), HAc (99.5%) and titanium isopropoxide, Ti(O<sup>i</sup>Pr)<sub>4</sub> (97%), were obtained from Alfa Aesar and used as received.

### 2.2 Synthesis

In a typical synthesis, Bi(NO<sub>3</sub>)<sub>3</sub>·5H<sub>2</sub>O (1 mmol, 485.1 mg) was dissolved in acetic acid (2 mL) to form a clear solution.

Na<sub>2</sub>WO<sub>4</sub>·2H<sub>2</sub>O (0.5 mmol, 164.9 mg) was added into the Bi source solution under vigorous stirring, which resulted in a white precipitate. Afterwards, Ti(O<sup>i</sup>Pr)<sub>4</sub> (0.2 mmol, 0.06 mL) was mixed with acetic acid (1 mL) and dropped into the as received slurry. After continuously stirring for 30 min, 20 mL of CTAB (1 mmol, 364.5 mg) aqueous solution was added into the above mixture. The suspension was continuously stirred for 24 h and then loaded into a 30 mL Teflon-lined autoclave. The autoclave was filled with the suspension to 80% of its total volume. Afterwards, the autoclave was heated in an oven at 145 °C for 24 h, and then naturally cooled down to room temperature, leading to the formation of a milky white precipitate. The precipitate was then collected, washed with distilled water and ethanol several times to remove ions and possible remnants, and dried in air at 80 °C for 12 h. The fabrications with different amounts of titanium precursors were done according to the above procedure. Single phase BiOBr and Bi<sub>2</sub>WO<sub>6</sub> were prepared according to previously reported methods.<sup>16,37</sup>

### 2.3 Characterization

X-ray diffraction (XRD) patterns of the products were recorded on a Bruker F8 Focus Powder XRD by using CuK $\alpha$  radiation ( $\lambda = 1.54 \text{ \AA}$ ). Scanning electron microscopy (SEM) images were obtained on a JSM 7000. Transmission electron microscopy (TEM) and high resolution TEM (HRTEM) characterizations were performed with a Tecnai F20 operated at 200 kV. BET measurements were carried out using a NOVA 4200e. UV-vis-NIR absorption spectra were recorded with an EVO300 PC. Photoinduced charge distribution was measured with a Kelvin probe force microscopy (KPFM) system equipped with backside LED illumination according to the method reported in the literature.<sup>40</sup>

### 2.4 Photocatalysis

The photocatalytic activities were evaluated by measuring the degradation of Rhodamine B (RhB) and methyl orange (MO) in an aqueous solution under visible light irradiation. The photocatalyst (100 mg) was added to a beaker containing 98 mL of deionized water. After ultrasonication, the dye aqueous solution (2 mL, 10<sup>−3</sup> M) was injected into the above solution to form a 2 × 10<sup>−5</sup> M dye aqueous solution. After continuously stirring in the dark for 30 min to ensure the establishment of an adsorption–desorption equilibrium, the photocatalytic test was conducted by irradiation with a 3 W LED lamp (400–405 nm, 4.0 mW cm<sup>−2</sup>). The concentration of the dye during the degradation was monitored using a UV-vis spectrometer.

## 3 Results and discussion

### 3.1 Structure and characterization

Fig. 1a is a typical SEM image showing that the MNCs possess a sphere-like structure with diameter ranging from 10 to 20 micrometers, and the spheres are built with thin flakes 10–30 nm in thickness and a few hundred nanometers in width. These thin flakes, just like 2-dimensional spikes, are aligned from the sphere center to the surface (Fig. 1b). Owing to the non-close packing and the relatively random arrangement of

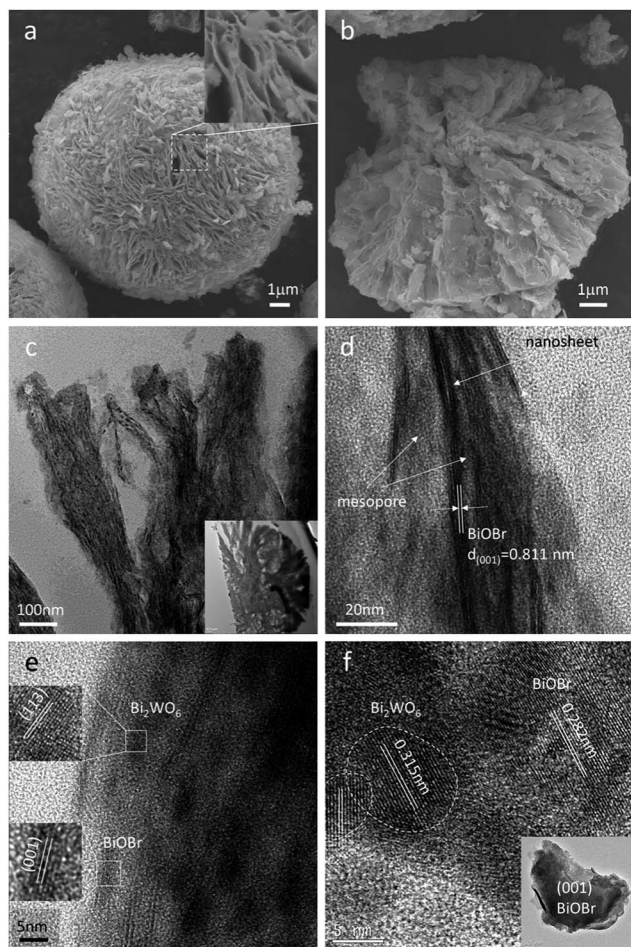


**Fig. 1** (a) SEM image of BiOBr–Bi<sub>2</sub>WO<sub>6</sub> MNCs showing the assemblage of thin flakes; the inset is the high magnification image. (b) SEM image of the cross-section of a microsphere, indicating the aligning direction of thin flakes. (c) TEM image of the MNCs, showing the mesoporous structure made by stacking of nanosheets; the inset is the overall morphology at low magnification, in which the sample was prepared by embedding the as-synthesized microspheres in epoxy resin and thinning. (d) HRTEM image of the MNCs, indicating the mesopores between adjacent BiOBr nanosheets and the BiOBr (001) lattice fringe. (e) HRTEM image showing the distribution of Bi<sub>2</sub>WO<sub>6</sub> with the grain fringe. (f) HRTEM image of BiOBr (001) plane; the inset is the low magnification image, showing the stacking of nanosheets; the BiOBr (001) facet is labeled. The sample in (f) was prepared by grinding the MNCs together with ethanol and ultrasonic processing to disassemble the microsphere. After that, the sample was dropped onto a copper grid for TEM observations.

the flakes, gaps and pores are formed through the entire microsphere, though the pore size and pore volume show an appreciable increase from the center towards the surface. Such conical-type porous structures would favor the penetration of liquids and allow quick transport of organic molecules. The TEM image at high magnification shown in Fig. 1c reveals that the thin flakes are composed of stacked nanosheets  $\sim 3$  to 5 nm in thickness. The HRTEM image shown in Fig. 1d taken by focusing on an open edge of the microsphere indicates that although nanosheets are arranged *via* oriented alignment, there are gaps of several nanometers between the adjacent BiOBr nanosheets. The gaps between the nanosheets form a mesoporous structure. Such a mesoporous structure on the one hand allows for the penetration and transport of solution, and on the other hand enables each BiOBr nanosheet to be exposed with the (001) plane for heterocatalytic reactions. HRTEM observations also reveal that the small Bi<sub>2</sub>WO<sub>6</sub> nanocrystals are dispersed between adjacent BiOBr nanosheets of exposed (001) surface (Fig. 1e and f). The XRD pattern of BiOBr–Bi<sub>2</sub>WO<sub>6</sub> MNCs shown in Fig. 2a can be indexed to two types of crystals and is in conformity with the tetragonal phase of BiOBr (JSPDS 09-0393) and orthorhombic Bi<sub>2</sub>WO<sub>6</sub> (JSPDS 73-1126). It should be noted that no titania compound or titanium elements were detectable in the MNCs, which was also confirmed by XPS analysis (Fig. S1<sup>†</sup>), though an appreciable amount of titanium alkoxide was introduced to the precursor solution for synthesis. According to the EDS analysis shown in Fig. S2,<sup>†</sup> the atomic ratio of Bi and W in the product is 3 : 1. Combining the atomic ratio of Bi : W determined by EDS analysis with the identification of phase components by XRD, it can be inferred that the molar ratio of BiOBr and Bi<sub>2</sub>WO<sub>6</sub> is roughly 1 : 1, which is in good agreement with the ratio of BiOBr and Bi<sub>2</sub>WO<sub>6</sub> introduced in the precursor solution.

It is also worth noting that, according to the XRD pattern shown in Fig. 2a, the BiOBr (001) facet in MNCs is well developed; this is in good agreement with the TEM observations. Moreover, from the XRD results, it can be seen that the crystallinity of Bi<sub>2</sub>WO<sub>6</sub> is not apparently affected by the Ti(O<sup>i</sup>Pr)<sub>4</sub> existing in the precursor solution. It can be proposed based on the previous study in the literature that H<sup>+</sup> ions are prone to adsorb on the O-terminated (001) surface of BiOBr in an acidic environment, and the strong binding interaction between the

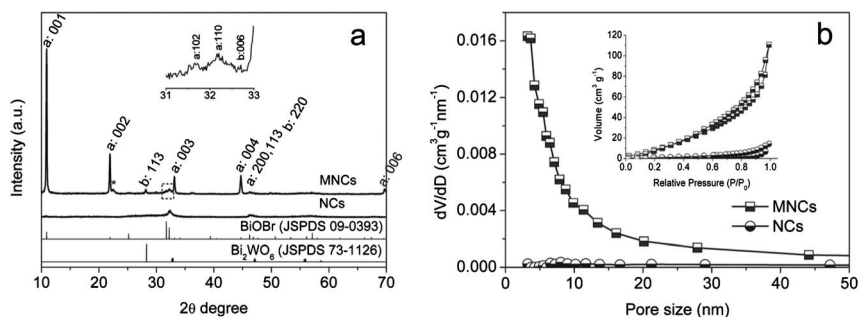


**Fig. 2** (a) XRD patterns of MNCs and of the Ti-free BiOBr–Bi<sub>2</sub>WO<sub>6</sub> nanosheet composites (NCs); the inset is the expanded scale in the range of 31–33° (2 $\theta$ ). (a) BiOBr, (b) Bi<sub>2</sub>WO<sub>6</sub>. The asterisk indicates the possible existence of tungsten trioxide. (b) Pore size distribution and N<sub>2</sub> adsorption–desorption isotherms using the BJH adsorption method.

$H^+$  ions and terminated oxygen on the (001) surface favors the formation of BiOBr nanosheets with a predominantly exposed (001) facet.<sup>33</sup> However, our XRD characterization reveals that no detectable peak arises from the BiOBr (001) facet when the BiOBr– $Bi_2WO_6$  nanosheet composites (NCs) were synthesized in acidic conditions ( $pH = \sim 1.2$ ) but with no  $Ti(O^iPr)_4$  involved. Instead, in the case of  $Ti(O^iPr)_4$  added in the precursor solution, the XRD patterns clearly show the formation of the BiOBr (001) plane (Fig. S3†). Although the exact mechanism for the formation of BiOBr nanosheets with predominant (001) facets in the presence of titanium alkoxide is unclear at this moment and requires further investigation, transition metal alkoxides are known to exert cross catalytic effects during hydrolysis and condensation reactions, which lead to different morphologies.<sup>41,42</sup> For example, when a small amount of titanium alkoxide or zirconium alkoxide is introduced to the silicon alkoxide system, the hydrolysis and condensation reactions of silicon alkoxide could be drastically accelerated and result in the formation of highly porous structures.<sup>42</sup> In our work, when the  $Ti(O^iPr)_4$  was substituted with  $Ti(OBu)_4$  and the same fabrication process was followed, a similar improvement in the crystallinity of BiOBr was observed (Fig. S4†), whereas a direct incorporation of  $TiO_2$  nanocrystals did not exhibit any detectable influence on both the morphology and crystallinity of BiOBr. Not only did the  $Ti(O^iPr)_4$  make a great impact on facets development, but also it played a critical role in the pore evolution of the product. For BiOBr– $Bi_2WO_6$  NCs synthesized without  $Ti(O^iPr)_4$ , no pores were observed on the nanosheets, and as a result, the specific surface area of NCs was low, about  $1.64\text{ m}^2\text{ g}^{-1}$ , as shown in Fig. 2b, Table 1 and Fig. S5a and b.† However, interestingly, it was found that adding a small amount of  $Ti(O^iPr)_4$  (5 mol% of Ti against Bi) in the reaction solution might induce partial formation of spherical assemblages (Fig. S5c and d†). When the amount of  $Ti(O^iPr)_4$  was increased to, for example, 10 mol% or more, complete microspheres were formed. A further increase of the  $Ti(O^iPr)_4$  did not lead to an apparent change in morphology (Fig. S5e–h†). However, the specific surface area increased significantly to  $52\text{ m}^2\text{ g}^{-1}$  when 20 mol%  $Ti(O^iPr)_4$  was added. It has also been found that the pore size of the BiOBr– $Bi_2WO_6$  MNCs decreased with increasing

amount of  $Ti(O^iPr)_4$  (Fig. 2b and Table 1). It has been suggested in the literature that the pores in a hierarchical structure arise from the spaces among the aligned nanoflakes.<sup>38,43</sup> CTAB as a template to induce the formation of BiOBr and  $Bi_2WO_6$  microspheres has been verified; yet high mesopore volume was difficult to obtain by the use of CTAB alone as surfactant.<sup>17,36</sup> In the absence of  $Ti(O^iPr)_4$ , the  $[Bi_2O_2Br_2]$  sheets can be mutually attracted due to van der Waals forces, which causes intimate contact and the formation of bulk BiOBr flakes. The  $Ti(O^iPr)_4$  and its derivatives existing in the reaction solution may alter the surface energy of BiOBr and  $Bi_2WO_6$  and affect the thermodynamics and kinetics of the aggregation and the degree of close stacking of individual nanosheets. It was reported that the  $TiO_6$  octahedral unit in the  $TiO_2$  colloidal cluster could be accommodated between the perovskite  $WO_6$  layer and  $[Bi_2O_2]$  sheets in  $Bi_2WO_6$ ,<sup>35</sup> and the  $TiO_2$  precursor could modify interface bonding through the reaction with the surface hydroxyl.<sup>44</sup> We accordingly infer that the titanium alkoxide acts a cross modifier through bridging the interface between BiOBr and  $Bi_2WO_6$ . In an acidic precursor solution, the surface of BiOBr and  $Bi_2WO_6$  clusters would be easily hydroxylated by adsorbing  $H^+$  ions onto the terminated O atoms of the  $[Bi_2O_2]$  unit. In view of adding  $Ti(O^iPr)_4$  into the reaction solution, the BiOBr and  $Bi_2WO_6$  clusters would be bridged through O–Ti–O bonds during the hydrolysis of titanium alkoxide. In addition, the hydrolysis of adsorbed  $Ti(O^iPr)_4$  on the O-terminated (001) surface of BiOBr may also favor the formation of the (001) facet. Thus, the space between the  $[Bi_2O_2Br_2]$  layers would be forced to expand by the presumably electrostatic repulsion and steric hindrance, and allow a dramatic increase in mesopore volume and exposure of the BiOBr (001) surface, as illustrated in Fig. 3. With increasing crystallinity of BiOBr by increasing temperature or by prolonging the holding time during the hydrothermal

**Table 1** Structural parameters of BiOBr– $Bi_2WO_6$  MNCs

Sample <sup>a</sup>	Surface area <sup>b</sup> ( $\text{m}^2\text{ g}^{-1}$ )	Pore size <sup>c</sup> (nm)	Pore volume <sup>c</sup> ( $\text{cm}^3\text{ g}^{-1}$ )
NCs	1.64	8.04	0.022
MNCs-T5	3.25	11.6	0.051
MNCs-T10	3.81	7.21	0.053
MNCs-T15	14.3	5.55	0.144
MNCs-T20	52.0	3.22	0.179
MNCs-T25	13.0	6.52	0.094
BiOBr	0.99	4.24	0.010
$Bi_2WO_6$	19.9	8.94	0.103

<sup>a</sup> BiOBr– $Bi_2WO_6$  samples with different  $Ti(O^iPr)_4$  contents, named as MNCs-Tx (x =  $Ti(O^iPr)_4$  molar fraction against Bi). <sup>b</sup> The Brunauer–Emmett–Teller (BET) method was utilized to calculate the specific surface area. <sup>c</sup> Average pore size and pore volume were derived from the adsorption isotherms by the Barrett–Joyner–Halenda (BJH) model.

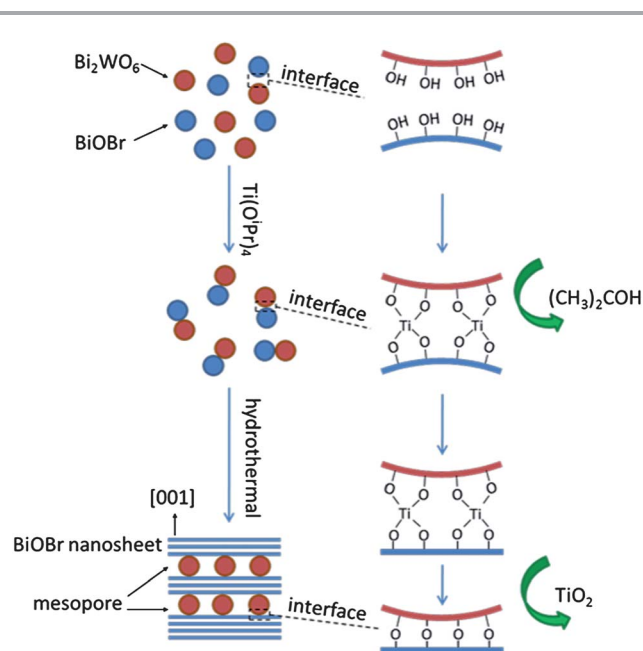


**Fig. 3** Schematic of the formation of the BiOBr– $Bi_2WO_6$  MNCs in the presence of  $Ti(O^iPr)_4$  during the hydrothermal process.

process, the Br ions may intercalate the  $[\text{Bi}_2\text{O}_2]$  layer and eliminate  $\text{TiO}_2$  clusters from the MNCs during the wash treatment. This can to some extent explain the mechanism of the formation of mesoporous nanosheets.

### 3.2 Kelvin Probe Force Microscopy (KPFM) analysis

To demonstrate the intricate relationship between the structure and photocatalytic function, we investigated photoinduced charge transfer properties of the MNCs and NCs of  $\text{BiOBr-Bi}_2\text{WO}_6$  by means of Kelvin Probe Force Microscopy (KPFM) equipped with a visible light source (405 nm, LED light) (Fig. S6†), in which the light intensity was adjusted by loading different resistors. By mapping the surface potential distribution, the charge separation can be characterized.<sup>40,45,46</sup> The experiment was conducted by dispersing a small amount of  $\text{BiOBr-Bi}_2\text{WO}_6$  disassembled thin flakes onto an ITO glass substrate, and then using visible light to excite the  $\text{BiOBr}$  and  $\text{Bi}_2\text{WO}_6$ . It was found that, no matter whether the light was on or off, the morphology and height of the sample as determined by atomic force microscopy (AFM) did not show apparent change (Fig. 4a and b). Under dark conditions, the surface potential of the nanosheets was found to be higher than that of the substrate (Fig. 4c), mainly due to the work function difference between these two materials. Under illumination, the local surface potential mapping exhibited a sharp contrast between MNCs and the ITO substrate (Fig. 4d), indicating more positive

charges on the surface of the MNCs. The photoresponse of the surface potential was confirmed to be reversible by cycling switch, and the result (Fig. 4e) strongly suggested that the change of surface potential originated from light illumination. Changing the wavelength of illumination to 465 nm gave no apparent change in the surface potential profile of the sample, because the absorption edge of  $\text{BiOBr-Bi}_2\text{WO}_6$  MNCs fell into the wavelengths around 440 nm and can only be excited by the light with a shorter wavelength (Fig. S7†). This is definite evidence indicating the separation of photogenerated electron-hole pairs, although the surface charge can be influenced by complicated environmental factors. Fig. 4f compares the surface potential profile of MNCs and NCs of  $\text{BiOBr-Bi}_2\text{WO}_6$  at the same light intensity. It can be seen that, for  $\text{BiOBr-Bi}_2\text{WO}_6$  MNCs, a sharp fluctuation of surface potential was observed when the cantilever scanned along the substrate-particle-substrate direction, while it was more flat for the NCs. Moreover, the surface potential difference increased with increasing illumination intensity, and the change in surface potential difference became more significant for  $\text{Ti}(\text{O}^i\text{Pr})_4$  introduced MNCs (Fig. 4g). As illustrated in Fig. 5a and b, the band edge potentials of CB and VB for  $\text{BiOBr}$  and  $\text{Bi}_2\text{WO}_6$  are well matched,<sup>38,47</sup> and this band offset leads to retardation of the electron-hole recombination rate.<sup>48</sup> These results clearly suggest that the MNCs possess better charge separation ability than their NC counterparts.

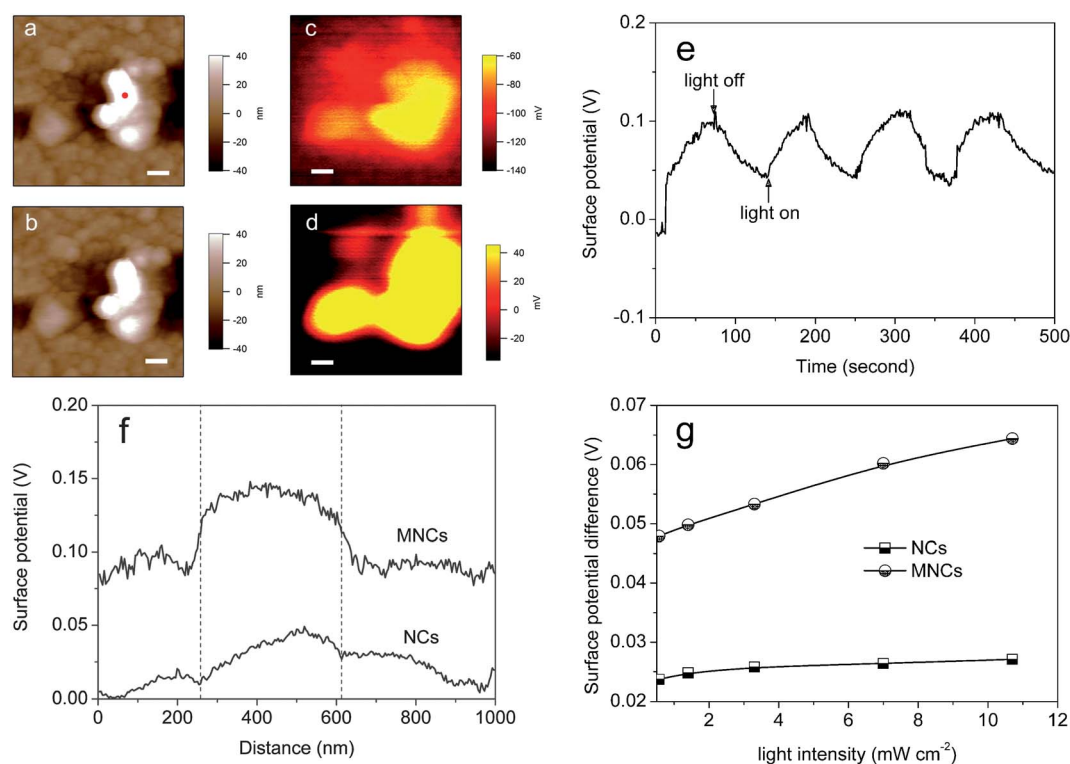


**Fig. 4** (a and b) AFM topographical images of the  $\text{Ti}(\text{O}^i\text{Pr})_4$  induced  $\text{BiOBr-Bi}_2\text{WO}_6$  MNCs immobilized on an ITO glass in the dark and under 405 nm LED irradiation, respectively. The red dot indicates the location where the surface potential was measured. (c and d) Surface potential mapping of the MNCs in the dark and under illumination, respectively. All the bars equal 200 nm. (e) Time dependent local surface potential cycle under on/off visible light illumination. (f) Surface potential profile of MNCs and NCs of  $\text{BiOBr-Bi}_2\text{WO}_6$ , measured at 3.3  $\text{mW cm}^{-2}$  intensity. The potential profiles are offset for clarity. (g) Averaged surface potential difference between the sample and the ITO substrate and its dependence on the light intensity.

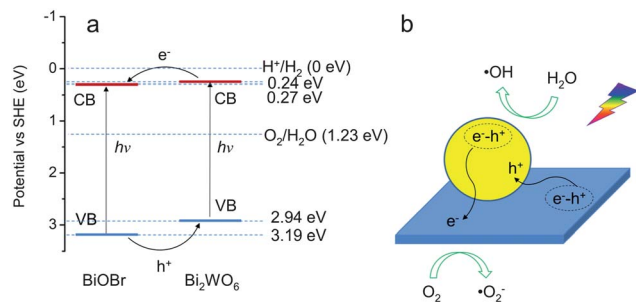


**Fig. 5** (a) Energy level of BiOBr and Bi<sub>2</sub>WO<sub>6</sub> using the normal hydrogen electrode (NHE) as a reference at pH 7. (b) Schematic illustration of the photocatalytic process involved in the BiOBr–Bi<sub>2</sub>WO<sub>6</sub> MNCs.

### 3.3 Photocatalytic decomposition of dye molecules

To prove the photocatalytic performance enhancement of the BiOBr–Bi<sub>2</sub>WO<sub>6</sub> MNCs, we examined the photocatalytic degradation of RhB and MO which act as probe reactions. Absorbance change in characteristic absorption peaks was monitored to evaluate the photocatalytic degradation activity. In our experiment, three reference samples were chosen to compare their activity: BiOBr, Bi<sub>2</sub>WO<sub>6</sub> and BiOBr–Bi<sub>2</sub>WO<sub>6</sub> NCs (with no Ti(O<sup>i</sup>Pr)<sub>4</sub> involved). Fig. 6a shows the time profiles of  $\ln(C/C_0)$  under visible light irradiation, where  $C$  represents the concentration of the dye at the illumination time and  $C_0$  the concentration at the adsorption–desorption equilibrium of the photocatalysts before illumination. After 40 min of visible-light irradiation, the percentages of RhB degradation were 24.5%, 52.5%, and 81.4% for Bi<sub>2</sub>WO<sub>6</sub>, BiOBr nanosheets and BiOBr–Bi<sub>2</sub>WO<sub>6</sub> NCs, respectively. It can be seen that almost 100% RhB was degraded in the case of Ti(O<sup>i</sup>Pr)<sub>4</sub> induced BiOBr–Bi<sub>2</sub>WO<sub>6</sub> MNCs. As illustrated by the UV-vis absorbance profile, no absorption bands appear in either the visible or ultraviolet region, suggesting the fast and thorough degradation of the dye (Fig. S8a<sup>†</sup>). Obvious blueshift of maximum absorbance emerged after irradiating the single phased BiOBr and BiOBr–Bi<sub>2</sub>WO<sub>6</sub> NCs, indicating incomplete decomposition of the dye molecules (Fig. S8b and c<sup>†</sup>). For the degradation of MO, the BiOBr–Bi<sub>2</sub>WO<sub>6</sub> MNCs showed significantly enhanced photocatalytic activities as well (Fig. S9<sup>†</sup>). In addition, considering that the photolysis of RhB under visible-light irradiation was very slow and RhB

cannot be degraded under dark conditions even in the presence of photocatalysts, the effective photocatalytic activity can be confirmed to originate from the BiOBr–Bi<sub>2</sub>WO<sub>6</sub> MNCs. Calcination at 500 °C for 2 h allowed a further growth of the grains and led to closing of the mesopores. As a result, the photocatalytic performance dramatically decreased. Therefore, it can be concluded that the observed activity enhancement is caused by the significantly high specific surface area and good charge separation ability of the BiOBr–Bi<sub>2</sub>WO<sub>6</sub> MNCs, which possess a unique mesoporous hetero-nanostructure. Neither Bi<sub>2</sub>WO<sub>6</sub> nor BiOBr showed highly efficient decomposition of the dye in solution under low light intensity LED irradiation because of the low charge separation efficiency, even though the as-synthesized Bi<sub>2</sub>WO<sub>6</sub> also had a high specific surface area and large mesopore volume (Table 1). Our study also revealed that BiOBr–Bi<sub>2</sub>WO<sub>6</sub> MNCs had a high photocatalytic activity under UV light illumination and demonstrated higher photocatalytic efficiency than the commercial TiO<sub>2</sub> nanoparticles (P-25).<sup>49</sup> A further increase in the content of Ti(O<sup>i</sup>Pr)<sub>4</sub> has been found to result in decreased photocatalytic activity, most likely due to the decreased surface area. The BiOBr–Bi<sub>2</sub>WO<sub>6</sub> MNCs also presented good stability and a long lifetime. Their catalytic activity did not show any appreciable decrease even after being used for 10 cycles (Fig. 6b).

## 4 Conclusions

In summary, a microsphere-shaped BiOBr–Bi<sub>2</sub>WO<sub>6</sub> composite photocatalyst with hierarchical nanostructure and large mesopore volume was achieved by using a facile hydrothermal synthetic route with a controlled fraction of Ti(O<sup>i</sup>Pr)<sub>4</sub>. The morphologies, structural properties, photoinduced charge separation and photocatalytic activities of the resultant BiOBr–Bi<sub>2</sub>WO<sub>6</sub> MNCs were investigated. In comparison with BiOBr–Bi<sub>2</sub>WO<sub>6</sub> NCs, the MNCs exhibited a much improved photocatalytic activity under visible light irradiation with low light intensity. The highly enhanced photocatalytic activity of the MNCs can be attributed to (1) the large specific surface area with hierarchical pore size and a highly exposed BiOBr (001) facet, which give rise to abundant sites for dye adsorption and occurrence of photocatalytic reactions, (2) the evidently enhanced charge separation efficiency which helps to increase

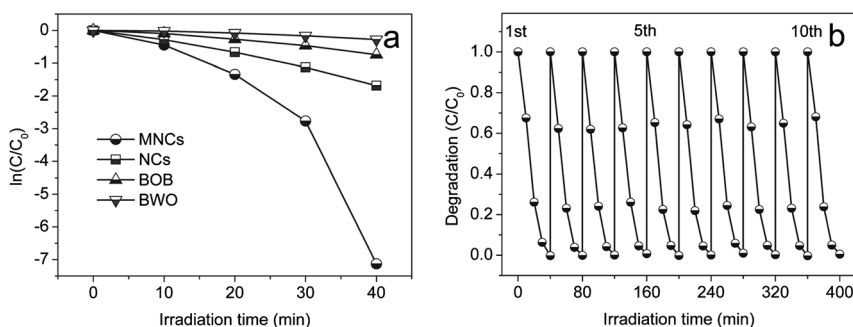


**Fig. 6** (a) Photodegradation of RhB in the presence of MNCs and NCs of BiOBr–Bi<sub>2</sub>WO<sub>6</sub>, BiOBr (BOB) and Bi<sub>2</sub>WO<sub>6</sub> (BWO) under exposure to a 3 W LED light (400–405 nm). (b) RhB cycling degradation curve of BiOBr–Bi<sub>2</sub>WO<sub>6</sub> MNCs.

the utilization of photoinduced charge carriers, yield long-lived reactive charges, and ultimately improve the dye degradation rate, and (3) high light harvesting efficiency of the BiOBr-Bi<sub>2</sub>WO<sub>6</sub> MNCs which results in efficient optical absorption and allows the material to work under very low light intensity illumination.

## Acknowledgements

The authors are grateful for the support of the U.S. Department of Energy, Office of Basic Energy Sciences, Division of Materials Sciences, under Award no. DE-FG02-07ER46467 (Q.F.Z.), the National Science Foundation (DMR 1035196 and CMMI 1030048), as well as the Royalty Research Fund (RRF) from the Office of Research at University of Washington and the National Nature Science Foundation of China (51225402). Y. L. Li would like to acknowledge Dr Feiyue Ma (ME Department, UW), Guozheng Shao and Huanxin Ju (Chemistry Department, UW) for the contribution of building up the LED optical system.

## Notes and references

- H. Tong, S. X. Ouyang, Y. P. Bi, N. Umezawa, M. Oshikiri and J. H. Ye, *Adv. Mater.*, 2012, **24**, 229–251.
- W. Y. Teoh, J. A. Scott and R. Amal, *J. Phys. Chem. Lett.*, 2012, **3**, 629–639.
- Y. Tachibana, L. Vayssieres and J. R. Durrant, *Nat. Photonics*, 2012, **6**, 511–518.
- S. H. S. Chan, T. Y. Wu, J. C. Juan and C. Y. The, *J. Chem. Technol. Biotechnol.*, 2011, **86**, 1130–1158.
- C. C. Chen, W. H. Ma and J. C. Zhao, *Chem. Soc. Rev.*, 2010, **39**, 4206–4219.
- Y. Li, W. Zhang, J. F. Niu and Y. S. Chen, *ACS Nano*, 2012, **6**, 5164–5173.
- S. Linic, P. Christopher and D. B. Ingram, *Nat. Mater.*, 2011, **10**, 911–921.
- T. R. Gordon, M. Cargnello, T. Paik, F. Mangolini, R. T. Weber, P. Fornasiero and C. B. Murray, *J. Am. Chem. Soc.*, 2012, **134**, 6751–6761.
- R. Su, R. Tiruvalam, Q. He, N. Dimitratos, L. Kesavan, C. Hammond, J. A. Lopez-Sanchez, R. Bechstein, C. J. Kiely, G. J. Hutchings and F. Besenbacher, *ACS Nano*, 2012, **6**, 6284–6292.
- Z. F. Bian, T. Tachikawa and T. Majima, *J. Phys. Chem. Lett.*, 2012, **3**, 1422–1427.
- S. G. Seo, C. Park, H. Kim, W. H. Nam, M. Jeong, Y. Choi, Y. S. Lim, W. Seo, S. Kim, J. Y. Lee and Y. S. Cho, *J. Mater. Chem. A*, 2013, **1**, 3639–3644.
- B. Lu, X. Li, T. Wang, E. Xie and Z. Xu, *J. Mater. Chem. A*, 2013, **1**, 3900–3906.
- W. L. Huang, *J. Comput. Chem.*, 2009, **30**, 1882–1891.
- Y. F. Fang, Y. P. Huang, J. Yang, P. Wang and G. W. Cheng, *Environ. Sci. Technol.*, 2011, **45**, 1593–1600.
- J. Xu, W. Meng, Y. Zhang, L. Li and C. S. Guo, *Appl. Catal., B*, 2011, **107**, 355–362.
- M. A. Gondal, X. F. Chang, M. A. Ali, Z. H. Yamani, Q. Zhou and G. B. Ji, *Appl. Catal., A*, 2011, **397**, 192–200.
- M. Shang, W. Z. Wang and L. Zhang, *J. Hazard. Mater.*, 2009, **167**, 803–809.
- G. F. Li, F. Qin, H. Yang, Z. Lu, H. Z. Sun and R. Chen, *Eur. J. Inorg. Chem.*, 2012, 2508–2513.
- Y. Huo, J. Zhang, M. Miao and Y. Jin, *Appl. Catal., B*, 2012, **111–112**, 334–341.
- H. F. Cheng, B. B. Huang, Z. Y. Wang, X. Y. Qin, X. Y. Zhang and Y. Dai, *Chem.–Eur. J.*, 2011, **17**, 8039–8043.
- Y. C. Feng, L. Li, J. W. Li, J. F. Wang and L. Liu, *J. Hazard. Mater.*, 2011, **192**, 538–544.
- J. Xu, W. Meng, Y. Zhang, L. Li and C. S. Guo, *Appl. Catal., B*, 2011, **107**, 355–362.
- H. J. Zhang, L. Liu and Z. Zhou, *RSC Adv.*, 2012, **2**, 9224–9229.
- J. Fu, Y. L. Tian, B. B. Chang, F. N. Xi and X. P. Dong, *J. Mater. Chem.*, 2012, **22**, 21159–21166.
- R. S. Yuan, S. L. Fan, H. X. Zhou, Z. X. Ding, S. Lin, Z. H. Li, Z. Z. Zhang, C. Xu, L. Wu, X. X. Wang and X. Z. Fu, *Angew. Chem., Int. Ed.*, 2012, **51**, 1–6.
- W. D. Wang, F. Q. Huang, X. P. Lin and J. H. Yang, *Catal. Commun.*, 2008, **9**, 8–12.
- L. Kong, Z. Jiang, H. Lai, R. J. Nicholls, T. C. Xiao, M. O. Jones and P. P. Edwards, *J. Catal.*, 2012, **293**, 116–125.
- Z. S. Liu, B. T. Wu, Y. B. Zhu, F. Wang and L. G. Wang, *J. Colloid Interface Sci.*, 2013, **392**, 337–342.
- D. Q. Zhang, M. C. Wen, B. Jiang, G. S. Li and J. C. Yu, *J. Hazard. Mater.*, 2012, **211**, 104–111.
- G. H. Jiang, X. H. Wang, Z. Wei, X. Li, X. G. Xi, R. B. Hu, B. L. Tang, R. J. Wang, S. Wang, T. Wang and W. X. Chen, *J. Mater. Chem. A*, 2013, **1**, 2406–2410.
- H. Gnayem and Y. Sasson, *ACS Catal.*, 2013, **3**, 186–191.
- G. C. Xi, J. H. Ye, Q. Ma, N. Su, H. Bai and C. Wang, *J. Am. Chem. Soc.*, 2012, **134**, 6508–6511.
- J. Jiang, K. Zhao, X. Y. Xiao and L. Z. Zhang, *J. Am. Chem. Soc.*, 2012, **134**, 4473–4476.
- L. S. Zhang, H. L. Wang, Z. G. Chen, P. K. Wong and J. S. Liu, *Appl. Catal., B*, 2011, **106**, 1–13.
- S. M. López, M. C. Hidalgo, J. A. Navío and G. Colón, *J. Hazard. Mater.*, 2011, **185**, 1425–1434.
- M. Ge, Y. F. Li, L. Liu, Z. Zhou and W. Chen, *J. Phys. Chem. C*, 2011, **115**, 5220–5225.
- Z. K. Cui, D. W. Zeng, T. T. Tang, J. Liu and C. S. Xie, *J. Hazard. Mater.*, 2010, **183**, 211–217.
- H. B. Fu, L. W. Zhang, W. Q. Yao and Y. F. Zhu, *Appl. Catal., B*, 2006, **66**, 100–110.
- H. F. Cheng, B. B. Huang, Y. Y. Liu, Z. Y. Wang, X. Y. Qin, X. Y. Zhang and Y. Dai, *Chem. Commun.*, 2012, **48**, 9729–9731.
- C. Liu, Y. J. Hwang, H. E. Jeong and P. D. Yang, *Nano Lett.*, 2011, **11**, 3755–3758.
- C. J. Brinker and G. W. Scherer, in *Sol-gel science: The physics and chemistry of sol-gel processing*, ed. L. Klein, Academic press, San Diego, 1990.
- C. M. Chan, G. Z. Cao, H. Fong, M. Sarikaya, T. Robinson and L. Nelson, *J. Mater. Res.*, 2000, **15**, 148–154.

- 43 Z. G. Xiong and X. S. Zhao, *J. Am. Chem. Soc.*, 2012, **134**, 5754–5757.
- 44 S. Ishchuk, D. H. Taffa, O. Hazut, N. Kaynan and R. Yerushalmi, *ACS Nano*, 2012, **6**, 7263–7269.
- 45 H. J. Chung, A. Yurtsever, Y. Sugimoto, M. Abe and S. Morita, *Appl. Phys. Lett.*, 2011, **99**, 123102.
- 46 W. Melitz, J. Shen, A. C. Kummel and S. Lee, *Surf. Sci. Rep.*, 2011, **66**, 1–27.
- 47 Z. Jiang, F. Yang, G. D. Yang, L. Kong, M. Jonesa, T. C. Xiao and P. Edwards, *J. Photochem. Photobiol., A*, 2010, **212**, 8–13.
- 48 H. J. Zhang, D. H. Wu, Q. Tang, L. Liu and Z. Zhou, *J. Mater. Chem. A*, 2013, **1**, 2231–2237.
- 49 R. J. Wang, G. H. Jiang, X. H. Wang, R. B. Hu, X. G. Xi, S. Y. Bao, Y. Zhou, T. Tong, S. Wang, T. Wang and W. X. Chen, *Powder Technol.*, 2012, **228**, 258–263.